RESEARCH ARTICLE | APRIL 01 2024

Investigation of the areas with high D07-band emission in multicrystalline silicon wafers using electron microscopy and hyperspectral photoluminescence imaging ⊖

Annett Thøgersen ✉ ⓘ ; Ingvild J. T. Jensen ⓘ ; Torbjørn Mehl ⓘ ; Ingunn Burud; Espen Olsen ⓘ ;
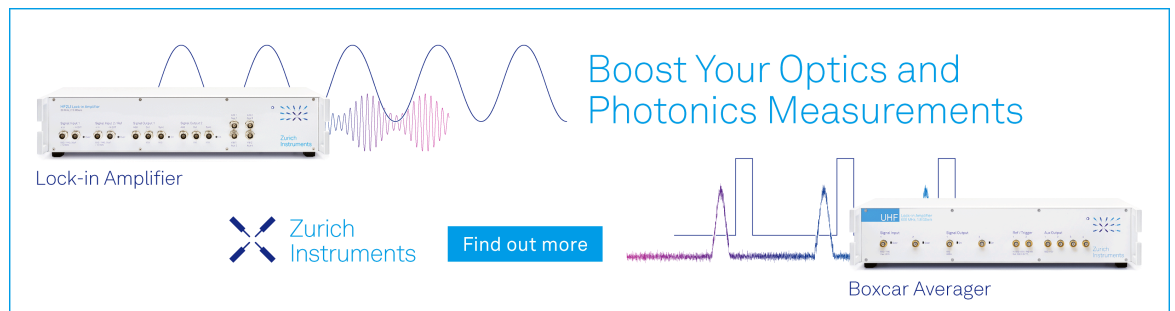Inga Gudem Ringdalen ⓘ ; Junjie Zhu ⓘ ; Rune Søndenå ⓘ

Check for updates

View Online   Export Citation

AIP
Publishing

Investigation of the areas with high D07-band emission in multicrystalline silicon wafers using electron microscopy and hyperspectral photoluminescence imaging (EP)

Annett Thøgersen,[1,a] (iD) Ingvild J. T. Jensen,[1] (iD) Torbjørn Mehl,[2] (iD) Ingunn Burud,[2] Espen Olsen,[2] (iD)
Inga Gudem Ringdalen,[3] (iD) Junjie Zhu,[4] (iD) and Rune Søndenå[4] (iD)

AFFILIATIONS

[1]SINTEF Industry, Materials Physics, Forskningsveien 1, 0373 Oslo, Norway
[2]Norwegian University of Life Sciences, NMBU, Universitetstunet 3, 1433 Ås, Norway
[3]SINTEF Industry, Materials Physics, Høgskoleringen 5, 7034 Trondheim, Norway
[4]Institute for Energy Technology, Department for the Solar Energy Instituttveien 18, 2007 Kjeller, Norway

[a]Author to whom correspondence should be addressed: annett.thogersen@sintef.no

ABSTRACT

This paper explores the fundamental structural origins of the 0.7 eV band emission peak, known as D07. The increased attention on these d-band emission lines originates mainly from the correlation between crystal defect and the intensified recombination of less dominant charge carriers. This association holds substantial importance, impacting not just the electronics sector but also raising concerns about reduced efficiency in silicon solar cells. By employing hyperspectral photoluminescence imaging, we pinpointed regions manifesting high D07 peak emissions on a microscopic scale. Subsequently, we conducted a structural investigation utilizing scanning electron microscopy and electron backscatter diffraction. Following this, we used a focused ion beam to extract areas of interest, allowing for a detailed characterization of the sample using high-resolution scanning transmission electron microscopy at the atomic scale. This approach aids in identifying defects and determining grain boundary orientation. In areas of high D07 band emission, we found Σ3{114}{101} grain boundaries decorated with two-layer fault twin and/or an extrinsic two-layer stacking faults. In addition, density functional theory calculations suggest oxygen impurities as a possibility for substitutional segregation to these types of defects. It is therefore plausible that the D07 line might be attributed to stacking faults featuring oxygen agglomerates.

I. INTRODUCTION

In the formation of high-performance multi-crystalline silicon, dislocations and grain boundaries arise during solidification, alongside impurities diffusing in from the crucible.[1] These material defects, such as grain boundaries, dislocations, and impurities, serve as centers for recombining holes and electrons, ultimately shortening the carrier lifetime in silicon wafers for photovoltaic (PV) use. Hydrogen, capable of bonding with and neutralizing various defects and impurities in silicon, emerges as a critical element.[2–8] Hydrogenation becomes a crucial step in enhancing the performance of multicrystalline silicon solar cell wafers due to the prevalence of extended crystal defects such as grain boundaries (GBs) and dislocation clusters. Nevertheless, not all defects respond equally to hydrogenation: dislocation clusters typically show minimal improvement, whereas hydrogenation tends to deactivate GBs. However, certain grain boundaries [small-angle, random-angle, and specific cases of coincidence site lattice (CSL) grain boundaries] remain reactive even after hydrogenation.[9] Hence, comprehending the structure and interfaces of these grain boundaries and defects becomes important. A deeper insight into the mechanism driving hydrogen passivation

of extended defects could yield optimized processes and heightened solar cell performance.

Drozdov and Partin initially described D-band emission lines in 1976, identifying sub-bandgap signals while investigating dislocations in Czochralski (Cz)-grown monocrystalline wafers.[10] These lines were later linked to emissions associated with dislocations in silicon.[10,11] The D-lines were categorized as D1 (0.812 eV peak), D2 (0.875 eV), D3 (0.934 eV), and D4 (1.000 eV).[10–13] D1 and D2 are often attributed to point defects in the strain field surrounding dislocations caused by the deformation process.[12,14] Conversely, D3 and D4 are predominantly associated with the defects themselves, as their emission peaks are observed around dislocation cores or sub-grain boundaries (sub-GBs).[12,15–17] In our prior study, we linked the prominent D3 peak to defects near $\Sigma 3$ GBs.[18] The interest in d-band emission lines stems from their association with crystal imperfections, causing amplified recombination of minority charge carriers. This correlation is concerning, affecting both the electronics industry and potentially diminishing silicon solar cell performance.[19]

An intriguing but less explored band emission peak, known as the D07 peak at 0.7 eV,[20] has predominantly surfaced at grain boundaries.[1] Additionally, it has been linked to iron (Fe-B) in p-type boron-doped Si wafers and associated with various grain boundaries, notably $\Sigma 9$, $\Sigma 27$, and random GB.[13,21] To conduct a detailed investigation into the precise positioning of the D07 peak on Si wafers, we adopted a comprehensive approach. This involved employing high spatial resolution photoluminescence (PL) spectroscopy maps, electron backscattered diffraction, and utilizing focused ion beam (FIB) for sectioning out samples. Furthermore, we conducted an in-depth analysis of the FIB lamella using high-resolution scanning transmission electron spectroscopy. These results was then compared to density functional theory (DFT) calculations.

II. EXPERIMENTAL

This investigation focused on exploring commercially available boron-doped high performance multi crystalline (HPMC) Si wafers with an approximate resistivity of $1\,\Omega$ cm. The process involved several steps: initially, the as-sawn wafers underwent damage etching in an HNA solution (comprising HF, nitric acid, and acetic acid). Next, a two-sided phosphorus emitter (approximately $70\,\Omega$/sq.) was diffused into the wafers using a $POCl_3$ tube-furnace. Before undergoing a simulated contact firing process (without metal contacts present) in a belt furnace, a hydrogen-rich SiN_X anti-reflective coating (ARC) was deposited on both sides of the wafers. Following this, the ARC and phosphorus emitter layers were removed using a new HNA solution. Verification of the wafers' hydrogenation through this process was confirmed using FT-IR.[22] To further refine the wafers, they were cleaned and surface passivated through the deposition of an $a-Si\!:\!H/SiN_X\!:\!H$-stack using plasma-enhanced chemical vapor deposition. This process typically yields surface recombination velocities of less than 5 cm/s.[23]

Hyperspectral photoluminescence (HSPL) images were obtained using a near-infrared (NIR) hyperspectral pushbroom camera (SWIR, Specim, Finland) on samples cooled to $90\,K$ with liquid nitrogen. A similar configuration was utilized in prior studies (see Refs. 20 and 24). The hyperspectral image underwent multivariate curve resolution (MCR) analysis to discern signals found in specific areas of the sample. Electron backscattered diffraction (EBSD) within the scanning electron microscope (SEM) was employed to study the grain boundary types and defects, specifically examining areas with high d-band emission. FIB was then used to prepare samples from selected regions of interest for transmission electron microscopy (TEM). Two types of samples were made, one in cross-sectional view (a JEOL JIB 4500 multibeam system), and one from plane view (made using a FEI Helios NanoLab DualBeam FIB). More details about the samples can be found in Sec. 1.1 in the supplementary material. An analysis of the atomic and electronic structure was performed utilizing a DCOR Cs probe-corrected FEI Titan G2 60-300 microscope, incorporating techniques such as fast Fourier transforms (FFT) for indexing the silicon structure and geometric phase analysis (GPA) with the FRWRtools plugin[25] in Digital Micrograph (Gatan Inc) to evaluate strain. Overall, this comprehensive investigation aimed to correlate material properties with specific spectral photoluminescence (SPL) peaks, utilizing a combination of microscopy, spectroscopy, and advanced analytical tools.
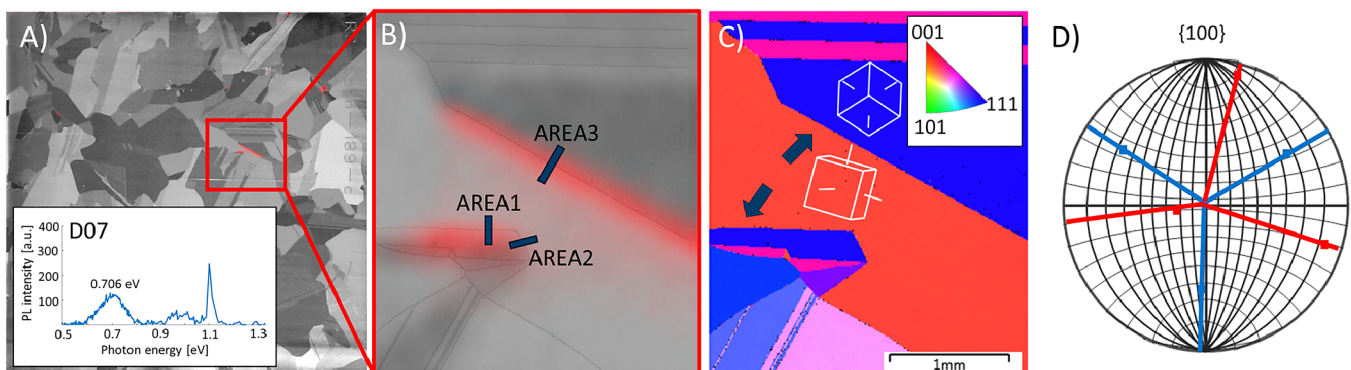
FIG. 1. (A) Optical image of the wafer with HSPL image of the spatial distribution of the D07 signal (in red) overlaid and an inset of the PL spectrum. (B) Band contrast image with HSPL image overlaid (with the location of the sectioned samples shown). (C) IPF in Z-direction EBSD image showing $\Sigma 3$ twins with the active slip system $\{1-10\}\langle 111\rangle$ (blue arrows show the investigated GBs). (D) Inverse pole figure map with the orientation of the red and blue grains in (C).
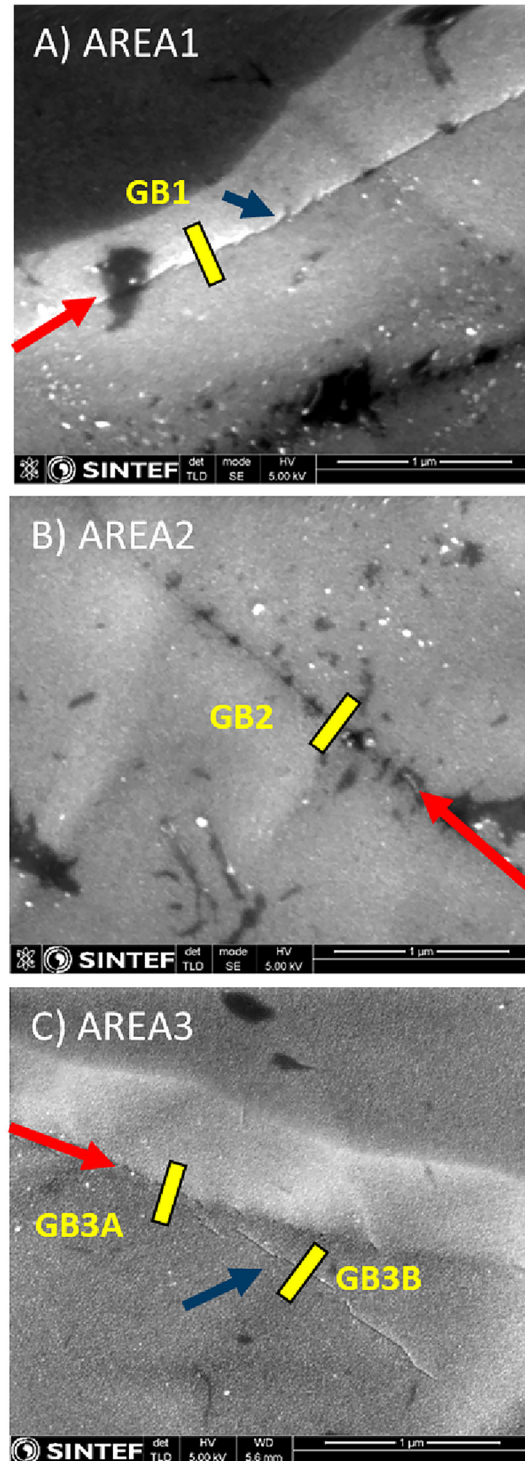
FIG. 2. SEM images with secondary electron (TLD) detector in high-resolution mode of (A) Area1, (B) Area2, and (C) Area3. Yellow areas showing the location of the FIB lamellas, and the red arrows shows the direction of the GBs.

DFT calculations were performed using the Vienna *ab initio* simulation package (VASP).[26,27] The Perdew–Burke–Ernzerhof (PBE) generalized gradient approximation (GGA)[28] functional was used. A convergence criterion in the change of the total energy of less than 10^{-5} eV was used for the ionic relaxations. The plane-wave energy cutoff used was 420 eV. A gamma sampling of 0.25 k points per Å was used for the Brillouin zone.
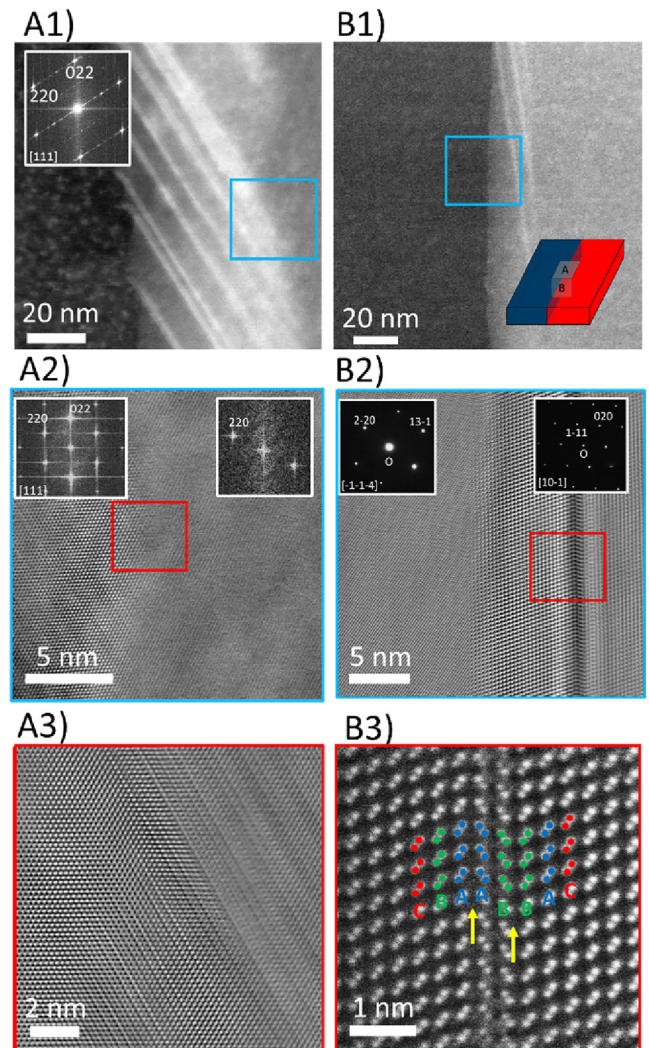
FIG. 3. STEM images of the grain boundary in AREA1 for both the plane view (A) and cross-sectional view (B) sample. (A1) ADF STEM image of AREA1 in plane view with FFT image as an inset. (A2) Higher resolution BF STEM image of the blue square in (A1) with FFT images as an inset. (A3) BF-STEM image of the red square in A2. (B1) ADF-STEM image of AREA1 in cross-sectional view, with the FIB section geometry related to the GB as an inset. (B2) Higher resolution BF image of the blue square in B1 with FFT as an inset. (B3) Higher resolution HAADF STEM images of the red square in B2 with the atomic positions of the Si dumbbells overlaid (the color is related to the type of lattice site). Yellow arrows shows the location of the twin plane.
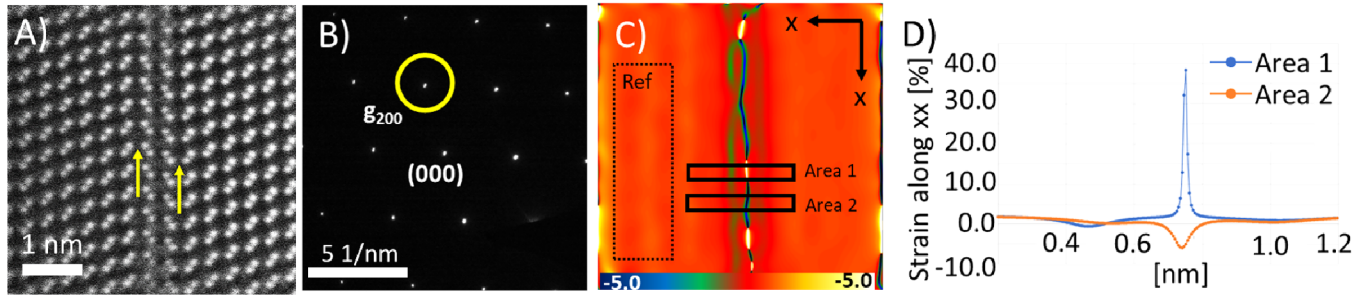
FIG. 4. (A) HR-STEM (HAADF) image of the GB in AREA1 (where the yellow arrows show the location of the twin planes), with the corresponding FFT pattern (B). (C) GPA strain analysis map of the ϵ_{xx} direction (g_{111}) of the defect, with the strain curve across the grain boundary in (D).

III. RESULTS

The D07 band emission peak was precisely located and mapped in a multicrystalline silicon wafer using HSPL. In Fig. 1(A), an optical image of the wafer showcases the D07 emission intensity depicted in red, with the mapped peak displayed as an inset. Positioned at 0.706 eV, the D07 band emission intensity stands out distinctly from the 1.1 eV band-to-band peak. Examining the image's contrast unveiled a microstructure characterized by coarse polygonal grains, frequently displaying distinct growth twin formations. However, at this scale, no explicit correlation between specific micro-structural features and PL emission was discernible. Zooming in on the selected area highlighted two regions emitting strongly in the D07 band spectral range, projected as elongated slices rather than spots or expansive regions. Figure 1(B), a SEM-EBSD band contrast image reveals the SPL D07 band emission intensity overlaid, distinctly outlining the presence of the D07 peak along two clear grain boundaries. Figure 1(C) showcases an inverse pole figure (IPF) EBSD map from the Z-direction of the same area, indicating that the grain boundaries in this region are Σ3{111}{001}. Notably, only two of these grain boundaries exhibit an SPL peak intensity of D07. Consequently, we have identified three areas of interest for further investigation: two areas demonstrating D07 peak intensity (AREA1 and AREA3) and one without (AREA2), as illustrated in Fig. 1(B).

We conducted a detailed investigation of the highlighted GBs depicted in Fig. 1 using SEM, presenting their corresponding images in Fig. 2. In these three SEM images, the GB is highlighted by a red arrow, and the selected regions for the FIB samples are indicated in yellow. AREA1 exhibits a GB where small defects are noticeable, originating directly from the grain boundary (highlighted with a blue arrow). Some charge differences are detected in the image close to the GB. Similarly, defects are also evident along the GB in AREA3, yet they seem to have extended further into the neighboring grain. In contrast, AREA2 displays no such defects or discernible intensity alterations in proximity to the GB.

To thoroughly investigate the GBs using scanning transmission electron microscopy (STEM), we created FIB sections specifically on the GBs. For both AREA1 and AREA2, we generated FIB sections in both plane view and cross-sectional view. However, for AREA3, we only produced a FIB section in cross-sectional view.

The images of the FIB lamellas can be found in Sec. 1.2 in the supplementary material.

Figure 3 presents both in-plane (A) and cross-sectional (B) views of AREA1 obtained through STEM images. In Fig. 3(A1), the plane-view annular dark field (ADF)-STEM image showcases a GB
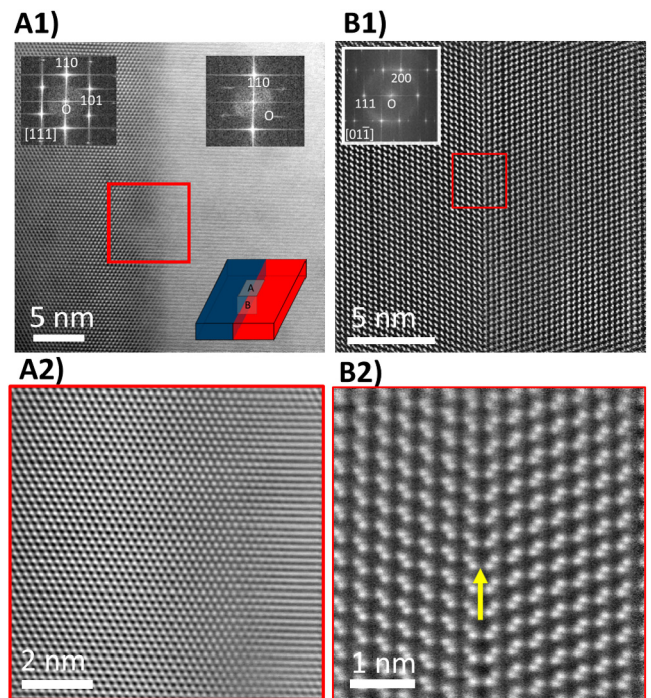
FIG. 5. High-resolution STEM images of the grain boundary in AREA2 for both the plane view (A) and cross-sectional view (B) sample. (A1) ADF STEM image from plane view, with FFT pattern and FIB section geometry related to the GB as an inset. (A2) Higher magnified BF STEM image of the red area in A1. (B1) HAADF STEM image of the cross-sectional view in AREA2. (B2) Higher resolution HAADF STEM image of the red area in B1 with yellow arrow showing the twin plane.

where defects extend into the adjacent grain. Moving to Figs. 3(A2) and 3(A3), these images offer a closer view of the highlighted region in Fig. 3(A1). Here, a higher magnification bright field (BF) STEM image is accompanied by a FFT pattern and inset displaying the FIB section geometry related to the GB. Notably, the left grain is oriented in [111] orientation, with defects starting in the left grain and extending into the right grain. These defects are observed from above, making them more discernible in the cross-sectional view.

Figure 3(B1) portrays the ADF STEM image of the cross-sectional view of the GB in AREA1, revealing defects that extend into the grain. Transitioning to Fig. 3(B2), a higher-resolution BF STEM image of the marked square in Fig. 3(B1) is presented, featuring FFT patterns as insets. Here, the right grain exhibits a [110] orientation, while the left grain is close to the [114] zone axis,

signifying a Σ3{114}{101} GB, similar to what is identified in AREA3 as illustrated in Sec. 1.3 in the supplementary material. Figure 3(B3) showcases a higher-resolution high angled annular dark field (HAADF) image of the indicated area in Fig. 3(B2). This image highlights a defect near the GB, containing two "twin boundaries." Referred to as a two-layer fault twin in previous studies,[29] this defect has also been denoted as an extrinsic two-layer stacking fault.[30,31]

To further investigate the defects observed in Fig. 3(B3), we conducted GPA, as illustrated in Fig. 4. The GPA strain analysis map focusing on the ϵ_{xx} direction (g_{111}) (utilizing the g_{200} reflection) reveals regions displaying both compressive and tensile strain fields, which are indicative of stacking faults.

The HRSTEM images of AREA2 are depicted in Fig. 5. In Fig. 5(A1), the in-plane view presents the GB, presenting the left
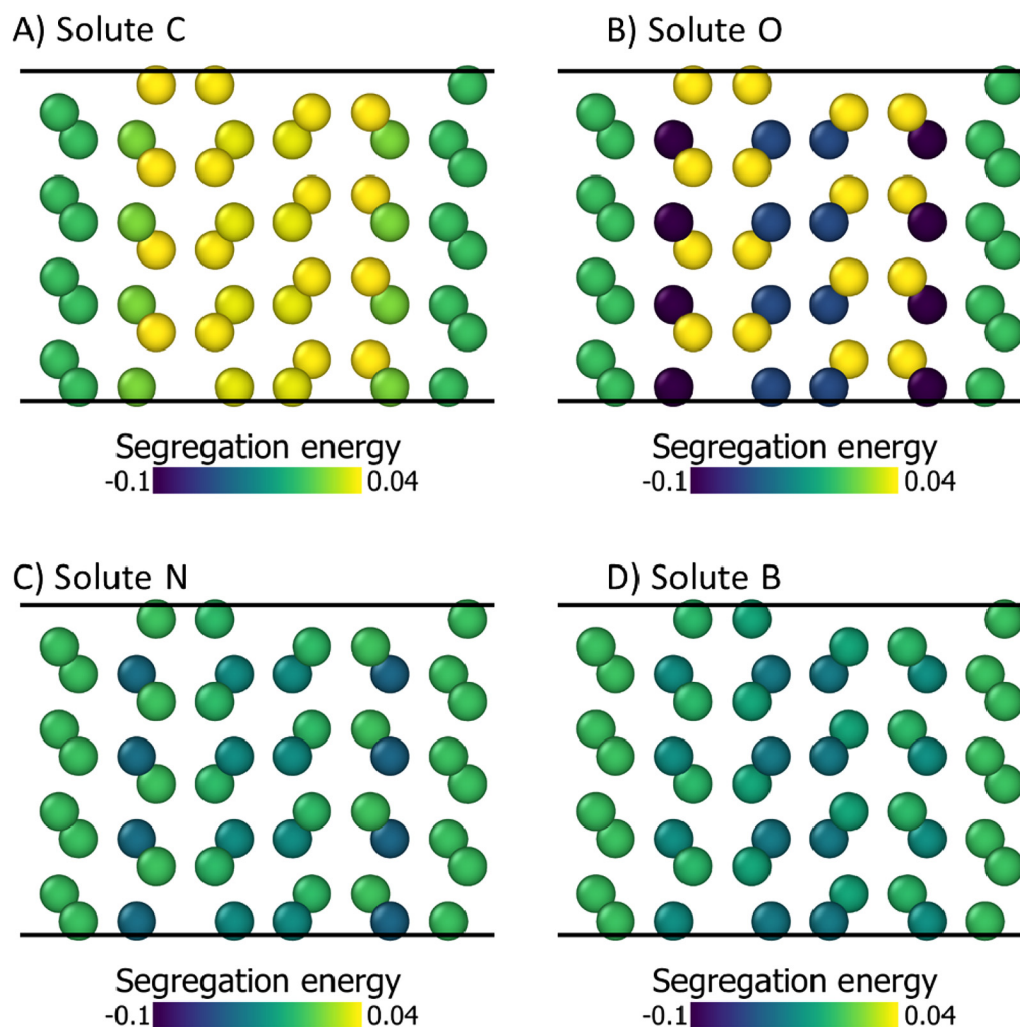
FIG. 6. Substitutional segregation energy at a two-layer fault twin found by DFT for impurity: (A) carbon, (B) oxygen, (C) nitrogen, and (D) boron. The energy scale of the segregation energy goes from −0.1 to 0.04 for all solute atoms.

grain in the [111] zone axis and the right grain near [001]. Notably, no defects are discernible along the GB in this orientation. Shifting to the cross-sectional view captured in the HAADF STEM image in Fig. 5(B1), the GB appears as an incoherent Σ3{111} twin boundary. A closer examination through the higher-magnification HAADF STEM image in Fig. 5(B2) reveals the absence of defects; instead, it displays a pure twin boundary without any additional strain.

Impurity segregation to the two-layer fault twin was calculated with DFT for light element impurities, such as carbon, oxygen, nitrogen, and boron, and the results are shown in Fig. 6. The images show the segregation energy when incorporating a solute atom into the lattice in a substitution position. When the segregation energy is negative, the position is the most stable. From these results, we can see that there may be positions near the defects that oxygen can find a favorable position. Yet, within these computations, we have solely accounted for substitutional segregation. However, regarding lighter elements, the diffusion process might present greater complexity, as there is a possibility of interstitial segregation, which could be more advantageous.

IV. DISCUSSION

The examined sample's three areas reveal from EBSD images identical Σ3 twin GBs along the z-direction. However, despite this, two of these areas exhibit notably high D07 emission intensity. A closer examination of the GBs shows that GB in AREA2 contains a flawlessly incoherent Σ3{111} twin boundary in cross-sectional view, devoid of defects visible in both cross-sectional and plane view images. Studies have indicated that segregation at Σ3{111} GB is unfavorable and electrically inactive,[32–34] thus posing no significant threat to the silicon wafer's performance.

Delving deeper into the crystal structure of the region with heightened D07-band emission uncovers an increased density of defects. In AREA1, we identified two twin boundaries adjacent to the Σ3{114}{101} GB, referred to as a two-layer fault twin and/or an extrinsic two-layer stacking fault. Our geometric phase analysis revealed that these defects introduce both compressive and tensile strain fields into the sample. DFT results indicate that only oxygen possesses the segregation energy suitable for substitutional segregation to the twin boundary. The D1 defect line has been suggested to be associated with oxygen precipitates.[35,36] Considering their proximity to the ingot's top, substantial amounts of oxygen impurities are expected, particularly in the multicrystalline sections. Consequently, it has been proposed that the D07 line could also stem from oxygen impurities.[19] Research has shown that dopant atoms can interact with stacking faults through Suzuki segregation, where dopants preferentially segregate to stacking faults.[37–39] By decorating the stacking fault with dopants/precipitates, the stacking fault energy (SFE) decreases, potentially leading to a higher density of stacking faults and twins. This mechanism might impede dislocation slip and enhance the material's fracture toughness.[39] Maji et al.[40] and Ohno et al.[41] conducted first principle calculations revealing that while the interstitial diffusion of oxygen to the Σ3111 Si grain boundary (GB) is not energetically favorable, the introduction of tensile strain induces a shift, making oxygen diffusion energetically favorable. The stacking

faults may therefore introduce tensile strain to the GB, which could be the driving force for oxygen diffusion. The D07 line may therefore be due to stacking fault with oxygen precipitates.

V. CONCLUSION

We have observed that regions exhibiting a prominent D07 band emission peak displayed the presence of stacking faults or twins near the GBs, introducing both compressive and tensile stresses to these boundaries. Notably, in cross-sectional view, the GB exhibited characteristics akin to a Σ3{114}{101} structure. Our DFT calculations suggested that considering substitutional segregation, oxygen emerges as the most probable dopant. Consequently, it is plausible that the manifestation of the D07 line might be attributed to stacking faults featuring oxygen precipitates.

SUPPLEMENTARY MATERIAL

The supplementary material section provides STEM images of the samples, FIB lamellas, and detailed STEM analysis of AREA3 in cross-sectional view.

AUTHOR DECLARATIONS

Conflict of Interest

The authors have no conflicts to disclose.

Author Contributions

Annett Thøgersen: Conceptualization (lead); Data curation (lead); Funding acquisition (equal); Investigation (lead); Methodology (lead); Project administration (equal); Resources (equal); Validation (lead); Visualization (lead); Writing – original draft (lead); Writing – review & editing (lead). **Ingvild J. T. Jensen:** Conceptualization (equal); Investigation (supporting); Writing – original draft (supporting). **Torbjørn Mehl:** Data curation (equal); Investigation (equal); Writing – original draft (supporting). **Ingunn Burud:** Conceptualization (equal); Funding acquisition (supporting); Supervision (supporting). **Espen Olsen:** Conceptualization (equal); Funding acquisition (supporting); Investigation (supporting); Supervision (supporting). **Inga Gudem Ringdalen:** Data curation (equal); Writing – original draft (supporting). **Junjie Zhu:** Conceptualization (supporting); Investigation (supporting). **Rune Søndenå:** Conceptualization (equal); Investigation (supporting); Project administration (lead); Resources (lead); Writing – original draft (supporting).

23 May 2024 11:53:26

DATA AVAILABILITY

The data that support the findings of this study are available from the corresponding author upon reasonable request.

REFERENCES

[1]A. Flø, I. Burud, K. Kvaal, R. Søndenå, and E. Olsen, AIP Adv. **3**, 112120 (2013).

[2]S. J. Pearton, J. W. Corbett, and M. Stavola, *Hydrogen in Crystalline Semiconductors* (Springer-Verlag, Heidelberg, 1992).

[3]B. Sopori, Y. Zhang, and N. M. Ravindra, J. Elec. Mater. **30**, 1616–1627 (2001).

[4]A. Azzizi, L. J. Geerligs, and D. H. Macdonald, in *Proceedings of 19th EUPVSEC* (WIP, Paris) (2004).

[5]B. J. Hallam, P. G. Hamer, S. Wang, L. Song, N. Nampalli, M. D. Abbott, C. E. Chan, D. Lu, A. M. Wenham, L. Mai, N. Borojevic, A. Li, D. Chen, M. Yong Kim, A. Azmi, and S. Wenham, Energy Procedia **77**, 799 (2015).

[6]M. S. Wiig, H. Haug, R. Søndenå, and E. S. Marstein, Energy Procedia **124**, 215 (2017).

[7]H. Haug, M. S. Wiig, R. Søndenå, B. Ryningen, G. Stokkan, and Ã. Mjøs, 36th EUPVSEC (WIP, Marseille) (2019).

[8]B. J. Hallam, P. G. Hamer, A. M. Ciesla née Wenham, C. E. Chan, B. Vicari Stefani, and S. Wenham, Prog. Photovolt.: Res. Appl. **28**, 1217 (2020).

[9]K. Adamczyk, R. Søndenå, G. Stokkan, E. Looney, M. Jensen, B. Lai, M. Rinio, and M. Di Sabatino, J. Appl. Phys. **123**, 055705 (2018).

[10]N. A. Drozdov, A. A. Partin, and V.D. Tkachev, Phys. Stat. Solidi B **83**, K137 (1977).

[11]S. Pizzini, M. Guzzi, E. Grilli, and G. Borionetti, J. Phys.: Condens. Matter **12**, 10131 (2000).

[12]R. Sauer, J. Weber, J. Stolz, E. R. Weber, K. H. Kusters, and H. Alexander, Appl. Phys. A **36**, 1 (1985).

[13]T. Mehl, I. Burud, E. Letty, and E. Olsen, Energy Procedia **124**, 107 (2017).

[14]G. M. Wyller, F. Schindler, W. Kwapil, J. Schön, E. Olsen, H. Haug, S. Riepe, and M. C. Schubert, IEEE J. Photovolt. **9**, 55 (2019).

[15]M. Tajima, Y. Iwata, F. Okayama, H. Toyota, H. Onodera, and T. Sekiguchi, J. Appl. Phys. **111**, 113523 (2012).

[16]E. C. Lightowlers and V. Higgs, Phys. Status Solidi A **138**, 665 (1993).

[17]H. T. Nguyen, M. A. Jensen, L. Li, C. Samundsett, H. C. Sio, B. Lai, T. Buonassisi, and D. Macdonald, IEEE J. Photovolt. **7**, 772 (2017).

[18]A. Thogersen, I. J. T. Jensen, J. S. Graff, I. Gudem Ringdalen, P. Almeida Carvalho, T. Mehl, J. Zhu, I. Burud, E. Olsen, and R. Søndena, J. Appl. Phys. **131**, 145703 (2022).

[19]E. Olsen, S. Bergan, T. Mehl, I. Burud, K. E. Ekstrøm, and M. D. Sabatino, Phys. Status Solidi A **214**, 1700124 (2017).

[20]D. Lausch, T. Mehl, K. Petter, A. Svarstad Flø, I. Burud, and E. Olsen, J. Appl. Phys. **119**, 054501 (2016).

[21]T. Mehl, M. Di Sabatino, K. Adamczyk, I. Burud, and E. Olsen, Energy Procedia **92**, 130 (2016).

[22]P. M. Weiser, E. Monakhov, H. Haug, M. S. Wiig, and R. Søndenå, J. Appl. Phys. **127**, 065703 (2020).

[23]H. Haug, R. Søndenå, M. S. Wiig, and E. S. Marstein, Energy Procedia **124**, 47 (2017).

[24]E. Olsen and A. Flø, Appl. Phys. Lett. **99**, 011903 (2011).

[25]C. T. Koch, see https://www.physics.hu-berlin.de/en/sem/software/software_frwrtools for *Frwrtools Plugin*.

[26]G. Kresse and J. Furthmüller, Phys. Rev. B **54**, 11169 (1996).

[27]G. Kresse and J. Furthmüller, Comput. Mater. Sci. **6**, 15 (1996).

[28]J. P. Perdew and Y. Wang, Phys. Rev. B **46**, 12947 (1992).

[29]S. Kibey, J. Liu, D. Johnson, and H. Sehitoglu, Acta Mater. **55**, 6843 (2007).

[30]B. C. D. Cooman, Y. Estrin, and S. K. Kim, Acta Mater. **142**, 283 (2018).

[31]P. Yu, P. Zhuang, J.-P. Chou, J. Wei, Y.-C. Lo, and A. Hu, Sci. Rep. **9**, 10940 (2019).

[32]D. Zhao and Y. Li, J. Alloys Compd. **712**, 599 (2017).

[33]P. Käshammer and T. Sinno, J. Appl. Phys. **118**, 095301 (2015).

[34]D. Ast and B. Cunningham, in *Silicon Processing for Photovoltaics I*, edited by C. P. Khattak and K. Ravi (Elsevier, 1985), Vol. 5 of *Materials Processing: Theory and Practices*, pp. 247–306.

[35]T. Mchedlidze, T. Arguirov, O. Kononchuk, M. Trushin, and M. Kittler, Phys. Status Solidi C **8**, 991 (2011).

[36]S. Pizzini, M. Acciarri, E. Leoni, and A. Le Donne, Phys. Status Solidi B **222**, 141 (2000).

[37]Y. Ohno, T. Taishi, Y. Tokumoto, and I. Yonenaga, J. Appl. Phys. **108**, 073514 (2010).

[38]H. Suzuki, J. Phys. Soc. Jpn. **17**, 322 (1962).

[39]X.-Y. Cui, H.-W. Yen, S.-Q. Zhu, R. Zheng, and S. P. Ringer, J. Alloys Compd. **620**, 38 (2015).

[40]R. Maji, E. Luppi, N. Capron, and E. Degoli, Acta Mater. **204**, 116477 (2021).

[41]Y. Ohno, K. Inoue, K. Fujiwara, K. Kutsukake, M. Deura, I. Yonenaga, N. Ebisawa, Y. Shimizu, K. Inoue, Y. Nagai, H. Yoshida, S. Takeda, S. Tanaka, and M. Kohyama, Appl. Phys. Lett. **110**, 062105 (2017).

23 May 2024 11:53:26